

1 Enhanced heating rate of black carbon above planetary  
2 boundary layer over megacities in summertime

3

4

5 Dantong Liu<sup>1,3</sup>, Delong Zhao<sup>2,3,6</sup>, Zhenzhen Xie<sup>4</sup>, Chenjie Yu<sup>7</sup>, Ying Chen<sup>8</sup>, Ping Tian<sup>2,3</sup>, Shuo  
6 Ding<sup>1</sup>, Kang Hu<sup>1</sup>, Douglas Lowe<sup>7</sup>, Quan Liu<sup>2,3</sup>, Wei Zhou<sup>2,3</sup>, Fei Wang<sup>2,3</sup>, Jiujiang Sheng<sup>2,3</sup>, Shaofei  
7 Kong<sup>5</sup>, Dawei Hu<sup>7</sup>, Zhenzhu Wang<sup>9</sup>, Deping Ding<sup>2,3</sup>

8

9

10 <sup>1</sup>Department of Atmospheric Sciences, School of Earth Sciences, Zhejiang University, Hangzhou, Zhejiang,  
11 China

12 <sup>2</sup>Beijing Weather Modification Office, Beijing, China

13 <sup>3</sup>Beijing Key Laboratory of Cloud, Precipitation and Atmospheric Water Resources, Beijing, China

14 <sup>4</sup> Huaian Meteorological Observatory of Jiangsu Province, Huaian, China

15 <sup>5</sup>Department of Atmospheric Sciences, School of Environmental Studies, China University of Geosciences  
16 (Wuhan), Wuhan, China

17 <sup>6</sup>School of Atmospheric Sciences, Nanjing University, Nanjing, China

18 <sup>7</sup>Centre for Atmospheric Sciences, School of Earth and Environmental Sciences, University of Manchester,  
19 Manchester M13 9PL, UK

20 <sup>8</sup>Lancaster Environment Centre, Lancaster University, Lancaster LA1 4YQ, UK

21 <sup>9</sup>Anhui Institute of Optics and Fine Mechanics, Chinese Academy of Sciences, Hefei, 230031, Anhui, China

22

23

24 **Abstract**

25 The fast development of a secondary aerosol layer was observed over megacities in eastern Asia  
26 during summertime. Within three hours, from midday to early afternoon, the contribution of  
27 secondary aerosols above the planetary boundary layer (PBL) increased by a factor of 3-5, and the  
28 coatings on the black carbon (BC) also increased and enhanced its absorption efficiency by 50%. This  
29 tended to result from the intensive actinic flux received above the PBL which promoted the  
30 photochemical reactions. The absorption of BC could be further amplified by the strong reflection of  
31 solar radiation over the cloud top across the PBL. This enhanced heating effect of BC introduced by  
32 combined processes (intensive solar radiation, secondary formation and cloud reflection) may  
33 considerably increase the temperature inversion above the PBL. This mechanism should be  
34 considered when evaluating the radiative impact of BC, especially for the polluted regions receiving  
35 strong solar radiation.

36 **Key words:** Black carbon, absorption enhancement, heating rate, cloud reflection

37

38

## 39 1. Background

40 The absorption of shortwave radiation, and consequential atmospheric heating effect, by black carbon  
41 (BC) has important impacts on the atmospheric radiative balance (Ramanathan and Carmichael,  
42 2008). In regions with high BC emissions, these climatic effects may be intensified by its strong lower  
43 atmosphere heating and surface dimming effect, which could alter the thermodynamic structure of  
44 the planetary boundary layer (PBL) (Babu et al., 2002; Ding et al., 2016). The absorption efficiency  
45 of BC, described as the absorption coefficient per unit mass of refractory BC (rBC), will be enhanced  
46 if coated with non-BC materials, through the lensing effect (Liu et al., 2017). In addition, the heating  
47 effect will depend on the actinic flux incidental on the BC particles, which could be significantly  
48 increased at higher altitudes, because less dimming will be caused by aerosol optical depth (Norris  
49 and Wild, 2009).

50 It has been demonstrated in modelling studies that the absorption capacity of BC depends  
51 considerably on the location of the BC layer relative to the cloud layer, e.g. the absorption will be  
52 significantly enhanced if BC layer is above the cloud layer due to strong reflection by cloud top,  
53 whereas below the cloud layer the dimming effect will reduce the solar flux deposited on the BC  
54 (Jacobson, 2012; Nenes et al., 2002). The position of the BC layer relative to cloud could be crucial  
55 to determine its impact on cloud microphysics by heating at different levels (Johnson et al., 2004;  
56 Koch and Del Genio, 2010). This study presents the aircraft in-situ measurements, including the full  
57 aerosol size distribution and BC size-resolved mixing state, throughout the PBL (containing cloud  
58 layers) and lower atmosphere over a megacity in eastern China during summertime. The  
59 measurements of vertical profiles were conducted during different times of the day to reveal the  
60 diurnal evolution of the heating impact of BC.

61

## 62 2. Measurements and data analysis

### 63 2.1 Instrumentation and Data Processing

64 The aircraft KingAir-350 was deployed (Liu et al., 2018) to conduct vertical profiles over three  
65 successive days in summertime (13<sup>th</sup> to 15<sup>th</sup> of July, 2018) over the Xuzhou megacity in Eastern China  
66 (Fig. 1a). Each flight will be referred to by the date (0713, 0714, and 0715) from now on. The  
67 meteorological parameters, including ambient pressure, temperature, relative humidity and wind  
68 speed/direction, were characterized in-situ by the AIMMS-20 (Aircraft Integrated Meteorological  
69 Measurement System, Aventech Research Inc), which was calibrated on an annual basis. The typical

70 aircraft speed was about  $250 \text{ km h}^{-1}$ , and the ascent and descent rates during profiles were  $\sim 2\text{--}5 \text{ ms}^{-1}$ .  
71 As shown in Fig. 1b, the morning (9am) and midday (11:30am) profiles were performed on 0713,  
72 while the midday (12:00pm) and early afternoon (14:00pm) profiles were on 0714 and 0715. Night  
73 flights were also performed on all three days. The profiles covered the time of the day receiving the  
74 most intensive solar radiation across the midday. HYSPLIT backtrajectory analysis (Draxler and Hess,  
75 1998) (Fig. 1a) using  $1^\circ \times 1^\circ$ , 3-hourly GDAS1 reanalysis meteorology, was performed to track the  
76 air mass histories for all profiles. Two more flight campaigns conducted over Beijing in 2016 winter  
77 and 2012 summer (Fig. 1b) are introduced (Zhao et al., 2019) to only support the phenomenon  
78 observed here but the detailed radiative transfer calculation is not performed.

79 A wing-mounted Passive Cavity Aerosol Spectrometer Probe (PCASP-100X, DMT Inc, USA) was  
80 used to measure the particle size distribution at diameter= $0.12\text{--}2.5\mu\text{m}$ , at a time resolution of 1s. A  
81 wired heater on top of the inlet, and the dry sheath flow, assured the particles measured by the PCASP  
82 were in a dry state, with  $\text{RH} < 40\%$  (Strapp et al., 1992). In addition, the aerosol inlet of the aircraft  
83 included a silicate dryer, so aerosol measurements inside the cabin were also dry. The particulate  
84 matter (PM<sub>1</sub>) used in this study is derived from the PCASP optically measured size distribution by  
85 assuming an average density of  $1.5 \text{ g m}^{-3}$  (Cross et al., 2007). The Aitken and accumulation mode  
86 particle at diameter= $6\text{--}520\text{nm}$  was measured by an Engine Exhaust Particle Sizer (EPS, TSI inc.) with  
87 time resolution of 1s. The aerosol scattering cross section ( $C_{sca}$ ) and asymmetry parameter ( $g$ ) for  
88 each size bin is calculated based on the PCASP-measured size distribution by assuming a refractive  
89 index  $1.50+0i$ . A fast cloud droplet probe (FCDP, SPEC inc.) (O'Connor et al., 2008) was used to  
90 measure the droplet size distribution at ambient RH. All of the aerosol data in cloud was screened out,  
91 based on the FCDP measured liquid water content (LWC)  $>0.001 \text{ g m}^{-3}$ , but the LWC is used to  
92 indicate the location of cloud layers.

93 The physical properties of BC were characterized by a single particle soot photometer (SP2, DMT  
94 inc.) (Schwarz et al., 2006; Zhao et al., 2015). The SP2 is able to measure the rBC mass and associated  
95 coating for each rBC-containing particle. The BC core size is measured at  $0.05\text{--}0.45\mu\text{m}$  and the  
96 remaining mass outside of the detectable range is obtained by a lognormal extrapolation (Fig. S4). As  
97 the actual coating thickness depends on both the rBC core and coated BC size, a metric of coating  
98 information in bulk, described as a mass ratio of coating/rBC, is used to represent the overall coating  
99 status of the particle ensemble during a given time period (Liu et al., 2014). Recent work shows this  
100 metric is able to represent the total mass of coatings associated with BC (Ting et al., 2018). The  
101 absorption cross section ( $C_{abs}$ , in  $\text{m}^2$ ) or  $C_{abs}$  normalized by rBC mass (MAC, in  $\text{m}^2\text{g}^{-1}$ ) could be  
102 calculated based on measured rBC core size-resolved mixing state (an example given in Fig. S10b)

103 via core-shell mixing rule using BC refractive index of 1.95-0.79i (Bond and Bergstrom, 2006) and  
104 coating refractive index of 1.50-0i (Liu et al., 2015).

105 Fig. S5 shows an example of all size distributions measured on 0714. The scattering coefficient ( $\sigma_{sca}$ )  
106 is obtained by integrating the number concentration ( $N(D)$ ) and  $C_{sca}$  for all PCASP bins; and the  
107 absorption coefficient ( $\sigma_{abs}$ ) is the integration of  $C_{abs}$  and BC number concentration  $N(D_c)$  for all SP2  
108 BC core size bins ( $D_c$  up to 0.6 $\mu$ m will include >95% of the total rBC mass in this study). The sum  
109 of both gives the extinction coefficient, as expressed in Equation (1):

$$110 \quad \sigma_{ext} = \sigma_{sca} + \sigma_{abs} = \int_{D=0.12\mu m}^{2\mu m} N(D)C_{sca}(D)dD + \int_{D_c=0.08\mu m}^{0.60\mu m} N(D_c)C_{abs}(D_c)dD_c \quad (1).$$

111 This calculation is performed for every 200m altitude bin using the mean PCASP size distribution.  
112 The single scattering albedo ( $SSA=\sigma_{sca}/\sigma_{ext}$ ) and asymmetry parameter ( $g$ ) are also obtained for  
113 each altitude bin. The aerosol optical depth - AOD( $h$ ) for each altitude bin ( $h$ ) is obtained from the  
114 altitude-integrated  $\sigma_{ext}(h)$ , as expressed in Equation (2):

$$115 \quad AOD(h) = \sigma_{ext}(h)\Delta h \quad (2).$$

116 The AOD, SSA and  $g$  as a function of altitude (Fig. S8) serve as inputs for the radiative transfer  
117 calculation given below.

118 Micro-pulse lidars at 532nm (MPL-4B, Sigmaspace Co., USA), were located at Huaian and Hefei  
119 (marked as black dots in Fig. 1a) to monitor the temporal evolution of aerosol layer. A Wind-Profile-  
120 Radar (Airda-3000, Airda Co., China) was located close to Xuzhou (34.402°N, 118.017°E) to measure  
121 wind profiles.

122

## 123 2.2 Calculation of BC absorption and heating rate

124 The actinic flux spectrum ( $\lambda=250-2550$ nm) was calculated using the pseudo-spherical version of the  
125 Discrete Ordinates Radiative Transfer Code (DISORT), as implemented in the libRadtran software  
126 package (Emde et al., 2016). In this study, the aerosol AOD, SSA and  $g$  used are the in-situ measured  
127 parameters based on the PCASP and SP2 measurements (see above) and calculated at each  $\lambda$ . The  $\lambda$ -  
128 dependent AOD is derived from the calculation based on the PCASP measurement, which is used as  
129 an input, expressed as:

$$130 \quad AOD(\lambda)/AOD(870)=0.16+20.6*\exp(-0.0037*\lambda) \quad (3),$$

131 where  $AOD(\lambda)/AOD(870)$  is the ratio of AOD at specified  $\lambda$  over that at  $\lambda=870\text{nm}$ .

132 The parametrization of cloud effect on actinic flux is according to (Hu and Stamnes, 1993) to convert  
133 the cloud microphysical properties to optical properties. The inputs used are the in-situ measured  
134 vertical profiles of LWC, and cloud cover set as 0.15 according to the aircraft camera (Fig. S5). For  
135 details of the settings for the radiative transfer calculation refer to Table S1.

136 The absorption power of BC is then calculated as the actinic flux multiplied by absorption coefficient  
137 integrated over all  $\lambda$  and BC core sizes, expressed in Equation (4):

$$138 \quad P_{abs} = \int_{D_c=50\text{nm}}^{800\text{nm}} \int_{\lambda=250\text{nm}}^{2550\text{nm}} F_{ac}(\lambda) \sigma_{abs,rBC}(\lambda, D_c) M_{rBC}(D_c) d\lambda dD_c \quad (4),$$

139 where  $\sigma_{abs,rBC}$  is the BC mass absorption cross section (in  $\text{m}^2 \text{g}^{-1}$ ), which is a function of incident  $\lambda$   
140 and BC core size ( $D_c$ ),  $M_{rBC}$  is the rBC mass concentration at each  $D_c$  bin (in  $\mu\text{g m}^{-3}$ ), multiplying  
141 both to obtain the absorption coefficient of rBC (in  $\text{Mm}^{-1}$ ), and the actinic flux ( $F_{ac}$ , in  $\text{mWm}^{-2}$ ) is  
142 calculated from the DISORT radiative transfer module. Integrating over all wavelengths ( $\lambda=250\text{-}$   
143  $2550\text{nm}$ ) and  $D_c$  range ( $50\text{-}800\text{nm}$ ) gives the BC absorption power in unit volume of air (in  $\text{mW m}^{-3}$ ).  
144 The absorption power deposition efficiency ( $P_{eff}$ ) is the  $P_{abs}$  normalized by rBC mass in  $\text{mW}/(\mu\text{g}$   
145  $\text{rBC})$ .

146

### 147 3. Results

148 Fig. 2 schematically shows the mechanism this study will illustrate, which is the enhanced heating  
149 rate of BC above the PBL, resulting from combined effects of enhanced secondary formation, BC  
150 coatings and cloud reflection on actinic flux at this layer. These are in detail discussed in the following.  
151 For guidance, besides main figures, in the supplement, Fig. S1 and S2 shows the temporal evolution  
152 of wind profiles and aerosol extinction respectively; Fig. S3 shows MODIS cloud and AOD images;  
153 Fig. S4 shows measured typical size distribution; Fig. S5, S6 shows the vertical profiles of  
154 meteorological parameters, particle number concentrations and BC-related properties, respectively.

#### 155 3.1 Meteorology

156 The flights from 13<sup>th</sup>-15<sup>th</sup> July followed very close to the same route (Fig. 1a). The flight region was  
157 about 200km away from the coast of the East Ocean and is influenced by sea-land breezes in  
158 summertime. The top of PBL could be determined by the aircraft in-situ measured temperature  
159 inversion and stable potential temperature (Fig. S5), with the dash lines showing the height of the

160 PBL (PBLH). Radar wind profiles (Fig. S1) showed diurnal variation of wind shear which also  
161 reflected the PBLH. In the PBL the oceanic easterly air flow dominated, and above the PBL was  
162 continental southwesterly airmass. The PBLH increased from ~0.5km to ~1.1-1.5km from morning  
163 to early afternoon due to stronger convective mixing through daytime surface heating. At night the  
164 height of wind shear top was significantly lowered to be ~200m, consistent with the aircraft in-situ  
165 measured shallow temperature inversion for the post-sunset flight (Fig. S5). The high pressure centred  
166 over the East Ocean, evident in the 700hpa geopotential height (Fig. 1c), led to southwesterly  
167 continental transport to the flight location. During all three flight days the synoptic condition  
168 maintained a similar pattern. The backtrajectory analysis (Fig. 1a) showed that the measured air  
169 masses were transported about 50km (0.2° in latitude) from the south to the flight region in three  
170 hours. The region within this distance was controlled by a similar synoptic system (Fig. 1c). This  
171 means the air masses observed at different time of the day (in 3 hours transport) could be generally  
172 deemed to have similar air mass origin and regional influence. The Beijing winter and summer  
173 campaigns also chose the flights without important regional transport or shift of sources, e.g. the  
174 variation of rBC mass loading was less than 20% in the lower free troposphere (Fig. S7), and the  
175 variation of rBC mass in the PBL was due to daytime boundary layer development when some rBC  
176 mass from ground sources could be transported upwards to higher level. The atmospheric processing  
177 is thus considered to be mainly at local scale for the results here.

178 Persistent cloud layers were observed in 0714 and 0715 during Xuzhou campaign, principally thin  
179 layers of cumulus humilis, with cloud coverage of about 15-25% according to the aircraft camera and  
180 MODIS visible cloud images (Fig. S3). The FCDP-measured LWC (Fig. S5) indicates the location  
181 of cloud layer. The presence of these layers may partly reduce the visibility of MODIS AOD data on  
182 0714 and 0715 (Fig. S3), whereas on 0713 the cloud was not as intense thus AOD data is fully visible.

### 183 184 3.2 Enhanced heating rate of BC above the PBL in early afternoon

185 Fig. S6 shows the vertical profiles of aerosol number concentration for both Aitken and accumulate  
186 mode particle, PM1 mass concentration and effective diameter ( $D_{eff}$ ) at 120-800nm. Note that on 0713  
187 the daytime profiles were from morning (9am) to midday (11:30am), whereas on 0714 and 0715 they  
188 were from midday (12:00pm) to early afternoon (14:30pm). The development of the PBL led to  
189 uplifting of aerosol from the surface, coming with some dilution effect for certain days, i.e. reduced  
190 surface concentration. The residue layer was observed at night above the shallow inversion layer (not  
191 on 0715 as no observed inversion). On 0714 and 0715 there were notable increases in PM1 by a factor

192 of 3-5 above the PBL (Fig. S4c), which occurred in 2-3 hours from midday to early afternoon. This  
193 came with a decrease of Aitken mode particle number concentration (Fig. S6a) and considerably  
194 increased particle size (Fig. S6d) by 20%. This increase of particulate mass was less pronounced on  
195 0713 when profiles were conducted from morning to midday. This phenomenon was further validated  
196 by two lidar measurements away from the flight area with distance of about 170km and 270km  
197 respectively. As Fig. S2 showed, the extinction profile from lidar measurements at both locations  
198 featured with a fast developed PBL from 12:00 to 15:00, in addition there was an aerosol layer formed  
199 above the PBL during this time. This wide spatial consistency confirmed the regional nature of this  
200 phenomenon. Given this growth occurred during the period when solar radiation is most intense, it is  
201 inferred that aerosol growth within this layer may be driven by photochemical processing of gaseous  
202 precursors.

203 Fig. 3a showed that there was no notable variation of rBC mass above the PBL from 12:00 to 14:30  
204 in both 0714 and 0715. The change in total particulate mass (PM<sub>1</sub>) normalized by the rBC mass could  
205 broadly reflect the formation of secondary aerosol mass, because rBC is always primary while the  
206 addition of extra PM<sub>1</sub> mass will be mainly controlled by secondary formation (assuming the variation  
207 in the relative emission factors of other species is not significant in this relatively short experimental  
208 period). The consistent PM<sub>1</sub>/BC ratio in the PBL (Fig. 3b) at different times of the day suggested  
209 well-mixed primary and secondary sources, whereas a remarkable increase of PM<sub>1</sub>/rBC occurred  
210 above the PBL from midday to early afternoon by a factor of 3-5, and this was also consistent with  
211 the lidar-measured extinction across the region (Fig. S2).

212 The coatings associated with rBC, indicated by the coating/rBC mass ratio (Fig. 3c), also increased  
213 by a factor of 3-5 similar to PM<sub>1</sub>/rBC from midday to early afternoon. The absorption efficiency of  
214 BC and the absorption enhancement relative to uncoated BC increased from 5% up to 50% (Fig. 3d).  
215 Both 0714 and 0715 showed consistent results whereas in 0713 this enhancement was not observed  
216 (Fig. S7) as the measurements were from morning to midday. The PM<sub>1</sub>/rBC and the coatings of BC  
217 above the PBL at night decreased compared to that in the early afternoon, consistent with the lidar  
218 extinction, and this in turn suggested the importance of solar radiation on the formation of secondary  
219 aerosol. There was an increase of RH from 60% to 70% on 0714 between profiles in midday and  
220 early afternoon, which was more likely from the moisture uplift through convective mixing as there  
221 was no obvious wind profile (Fig. 1) or air mass shift (according to backtrajectory analysis). This  
222 may cause more significant increase of PM<sub>1</sub> and particle size (Fig. S6) compared to that on 0715,  
223 because more water molecular could also promote photochemical reactions and allow more semi-  
224 volatile species to condense (Donahue et al., 2006). There was no obvious variation of RH on 0715



225 but still showed significant enhancement of secondary species, for which the sole photochemical  
226 reaction tended to dominate. There was no solar irradiance increase from morning to midday on 0713  
227 thus no obvious secondary species formed. The results over Beijing in summer ((Zhao et al., 2019),  
228 Fig. 2) also confirmed the strong enhancement of BC coatings above the PBL in 2-3 hours evolution  
229 time by a factor of 2-3 occurring in the early afternoon, however was at a lower scale compared to  
230 Xuzhou, and this may result from a drier air mass ( $RH < 60\%$ , Fig. S5) in the FT for northern cities;  
231 whereas in Beijing winter this enhancement was significantly reduced with coating enhancement less  
232 than a factor of 1.5 or even decreased from midday to early afternoon (Fig. 4), which may be due to  
233 the reduced solar radiation and enhanced AOD dimming effect in winter (given the winter flights  
234 were conducted during a heavily polluted period with surface rBC mass loading  $> 4 \mu\text{g m}^{-3}$ ). A recent  
235 study conducted over Korea (Lamb et al., 2018) also indicated some enhanced coating thickness of  
236 BC above the PBL (in Fig. 4b at about 800hpa compared to 100hpa), whereas the mixing state of BC  
237 at higher altitude was more influenced by synoptic conditions. The enhanced coating of BC above  
238 the boundary layer therefore tends to be a general phenomenon for the site where intensive solar  
239 radiation is received above the PBL.

240 The observations here showed strong enhancements for secondary formation, BC coatings and  
241 absorption above the PBL in the hours with most intense solar radiation, however these enhancements  
242 were less pronounced in the PBL. This could be caused by strong photochemical activities above the  
243 PBL, while the increased aerosol optical depth may have a significant optical shielding effect in the  
244 PBL (Prabha and Hoogenboom, 2009; Streets et al., 2006). Radiative transfer calculations (Fig. S9)  
245 show that direct solar irradiance was reduced, especially within the PBL, by adding the measured  
246 aerosol loadings, whereas the downward diffuse irradiance was enhanced above the PBL due to  
247 increased particle size. The overall actinic flux thus showed significant enhancement above the PBL,  
248 compared to within the PBL, due to the aerosol loading (especially for the early afternoon in 0714  
249 and 0715). As Fig. 3b shows, the absolute absorbing power of BC was largely determined by the rBC  
250 mass loading, with heating rate 0.3-0.5 K/d in the PBL, while 0.1-0.18 K/d above the PBL. The power  
251 deposition efficiency ( $P_{eff}$ , as normalized by rBC mass) depended on the absorption efficiency of BC  
252 (MAC). In the PBL, the clear-sky  $P_{eff}$  6-8 mW/( $\mu\text{g rBC}$ ) was broadly within that measured in a North  
253 American city  $7 \pm 2.5 \text{ mW}/(\mu\text{g rBC})$  (Schwarz et al., 2009). Corresponding with the increase of BC  
254 coatings from midday to early afternoon, the  $P_{eff}$  showed an enhancement of up to 30% from  $\sim 7.0$  to  
255  $9.5 \text{ mW}/(\mu\text{g rBC})$  above the PBL from midday to early afternoon.

256 The presence of cloud layers above the PBL further altered the irradiance, i.e. enhancing the dimming  
257 at lower level but increasing the reflectance above the cloud layer (Fig. 5a). The thin cloud layer in

258 this study was mainly cumulus humilis with 15-25% cloud cover and LWC 0.1-0.3 g m<sup>-3</sup>. The cloud  
259 layer enhanced the  $F_{ac}$  above the PBL by 30% but weakened the  $F_{ac}$  below the PBL by 15%. This  
260 study finds the  $P_{eff}$  above the PBL will be further enhanced by 10% if considering the cloud coverage  
261 of 15% (Fig. 5c). Note that the cloud fraction is only an approximate estimate here but the  $F_{ac}$  will be  
262 further amplified if more cloud coverage. The absorption enhancement due to cloud reflection was  
263 previously studied for the BC above oceanic stratocumulus (Johnson et al., 2004) but this study  
264 provides the direct evidence. It should be also noted that the patchy nature of the cloud layer (Fig. S3  
265 and S5) may have allowed aerosols or precursors to penetrate the cloud layer, in order to form a BC  
266 layer with significant secondary coatings above the cloud layer, which may explain the cases for this  
267 study.

268

#### 269 4. Discussion and Conclusion

270 In this study, the fast formation of a secondary aerosol layer was observed during summertime: within  
271 three hours from midday to early afternoon, the contribution of secondary aerosol above the planetary  
272 boundary layer (PBL) increased by a factor of 3-5. This is likely due to the higher rates of  
273 photochemical processing at these altitudes, which is suppressed in the PBL due to dimming caused  
274 by the high AOD. The secondary species formed by this processing will condense on the BC and  
275 increase its coating content, leading to an enhancement of absorption efficiency by 50%.  
276 Consequently, the absorbing power deposited on the BC will be enhanced by combined effects of  
277 increased coatings and solar flux. These processes are schematically illustrated in Fig. 2. The results  
278 here are consistent with the chamber simulation study by (Peng et al., 2016) that a BC  $E_{abs}$  of ~50%  
279 occurred in 2-3 hours' ageing time during pollution condition. In addition, the solar flux received  
280 above the PBL as in this study may be more intensive than that on the ground because of less AOD  
281 dimming effect in addition to the cloud reflection above the PBL.

282 Cloud layers regularly form on top of the PBL in this region, and strong solar reflection by cloud top  
283 will significantly increase the actinic flux received by the BC above the cloud layer, further  
284 amplifying the amount of solar radiation absorbed by the BC. Given the strong solar radiation in  
285 summertime, all of these processes will occur in a short time scale. This strong heating effect of BC  
286 introduced by combining processes (intensive solar radiation, secondary coatings and cloud reflection)  
287 would considerably increase the temperature above the PBL, which may introduce feedback effects  
288 and accumulate more pollutants across this layer, further promoting the secondary formation.  
289 Previous study found the absorbing aerosols above the cloud may stabilize the underlying layer and

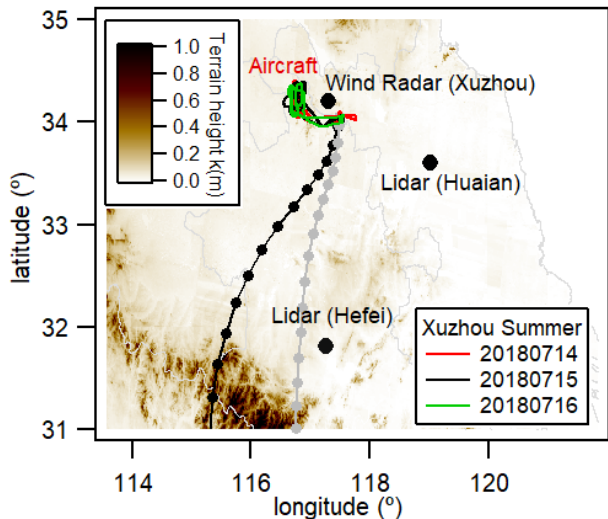
290 tend to enhance the cloud coverage below (Brioude et al., 2009), which may in turn enhance this  
291 feedback. This mechanism raised in this study should be considered when evaluating the BC heating  
292 effect at polluted region rich in BC and precursors, especially in summertime when solar radiation is  
293 strong. Further chemical measurements in gas and aerosol phase are also needed to elucidate the  
294 complex interactions over the top of the PBL.

295

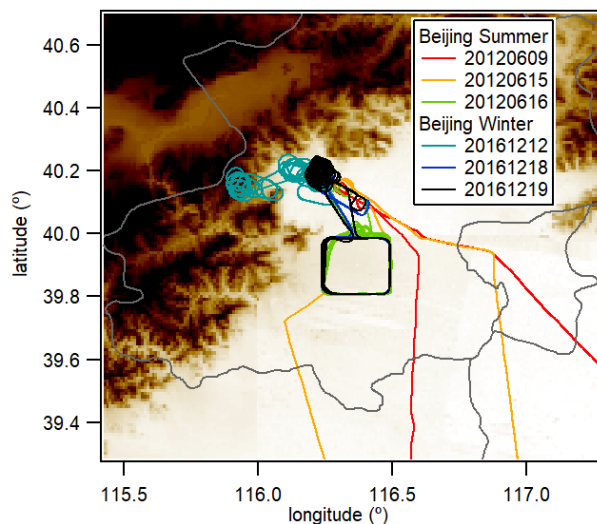
296 **Figures and captions**

297

298 (a)

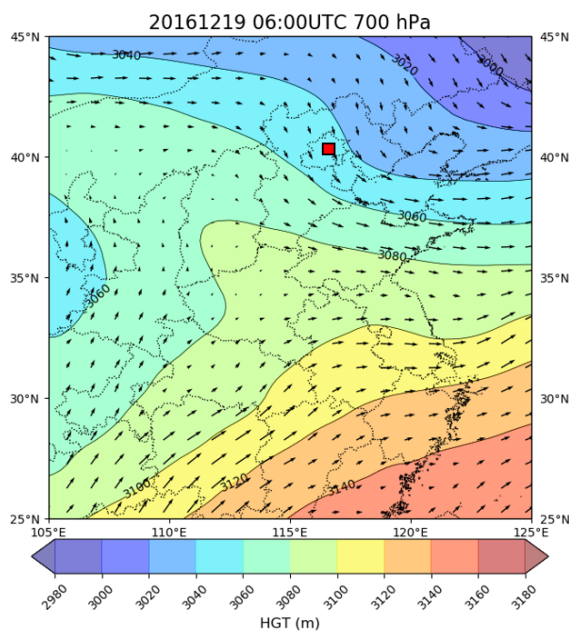
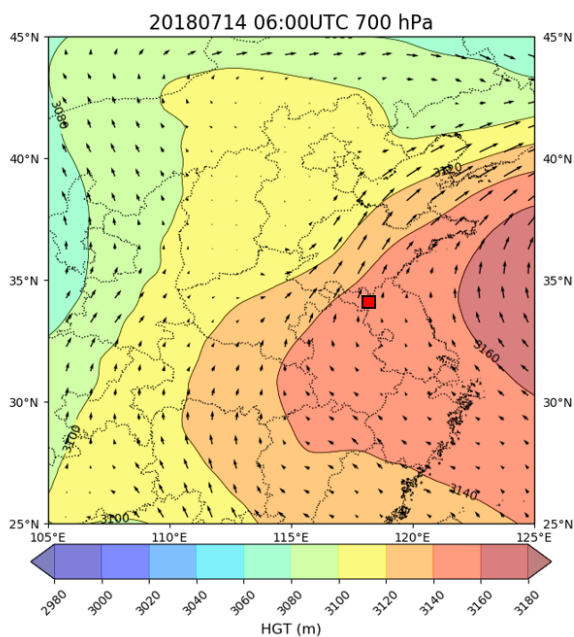


(b)



299

300 (c)

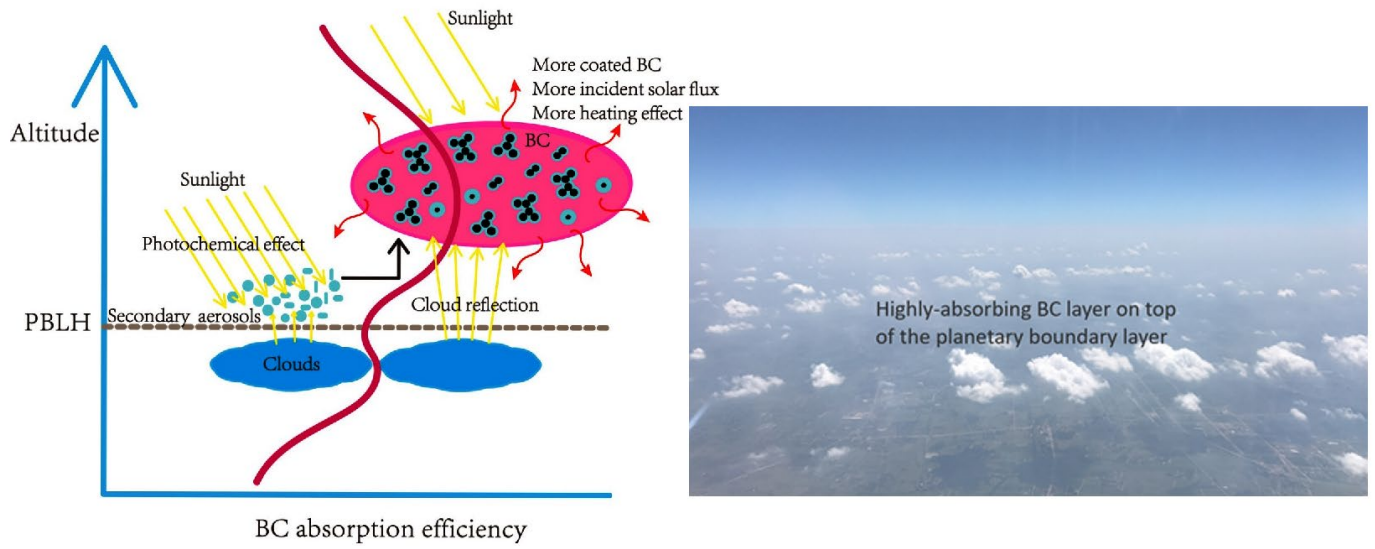


301

302

303 Fig. 1. (a) Flight tracks (coloured by aircraft altitude), locations of lidars in Huaian and Hefei, and  
 304 wind profile radar in Xuzhou (indicated by black dots). The black and grey lines show the  
 305 backtrajectories initialized at altitudes of 1.5km (above the PBL) and 0.5km (in the PBL) respectively,  
 306 each dot indicating a 1h time interval. (b) Flight tracks for Beijing 2012 summer and 2016 winter  
 307 campaigns. c) geopotential height in the free troposphere (at 700hpa) for Xuzhou and Beijing, the red  
 308 marker on each plot indicates the location of profiles.

309



310

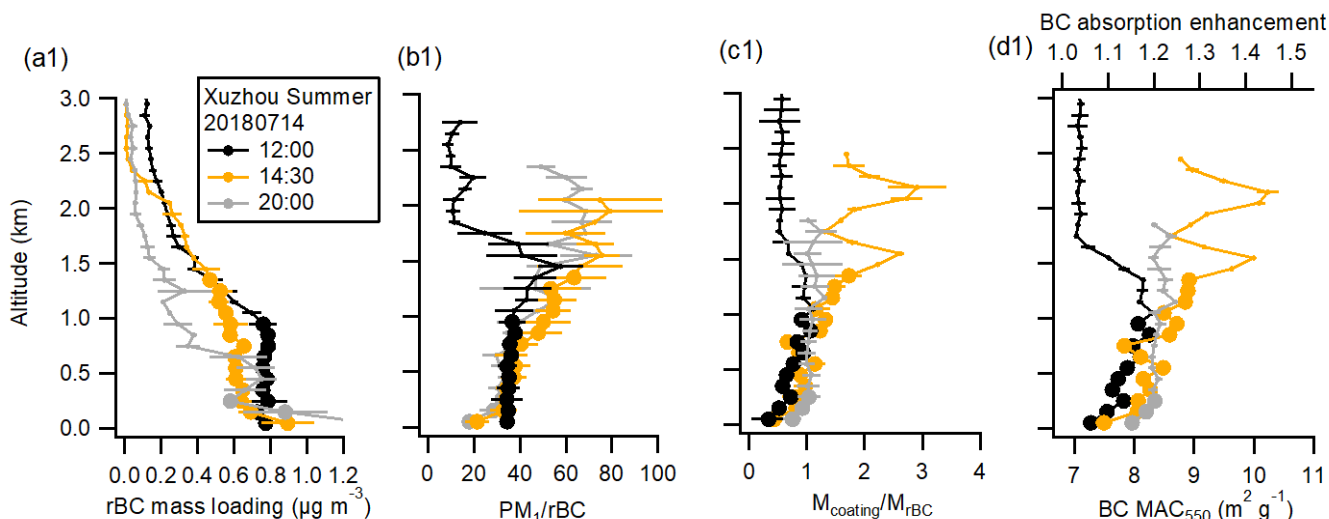
311

312 Fig. 2. Schematics and image illustrating the enhancement of BC heating effect above the PBL,  
313 resulting from the combined effects of enhanced secondary formation, BC coatings and cloud  
314 reflection above the PBL.

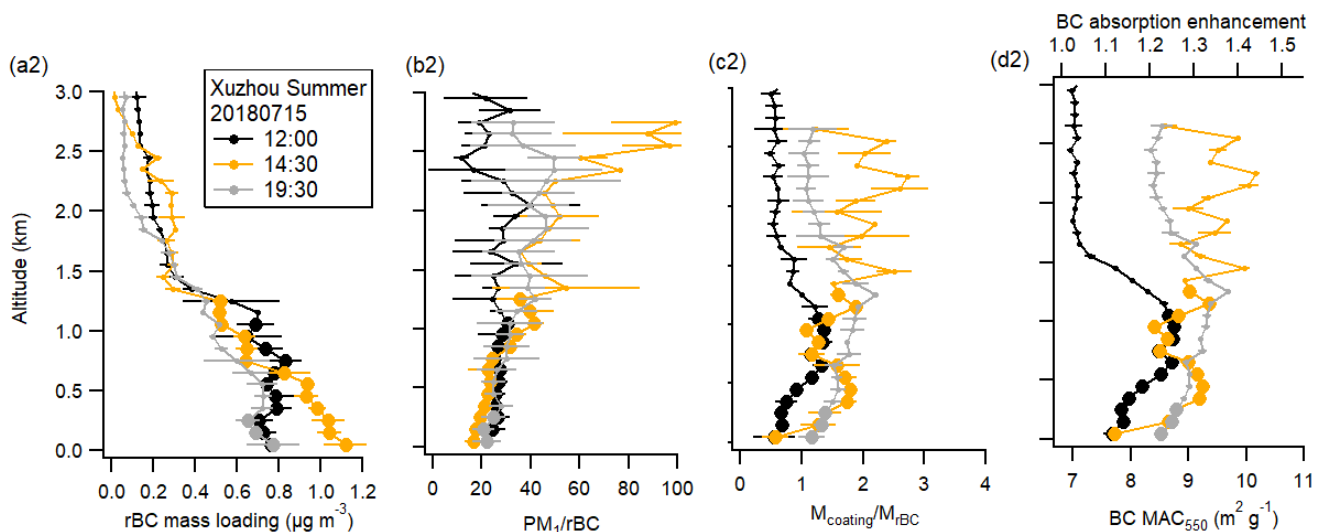
315

316

317



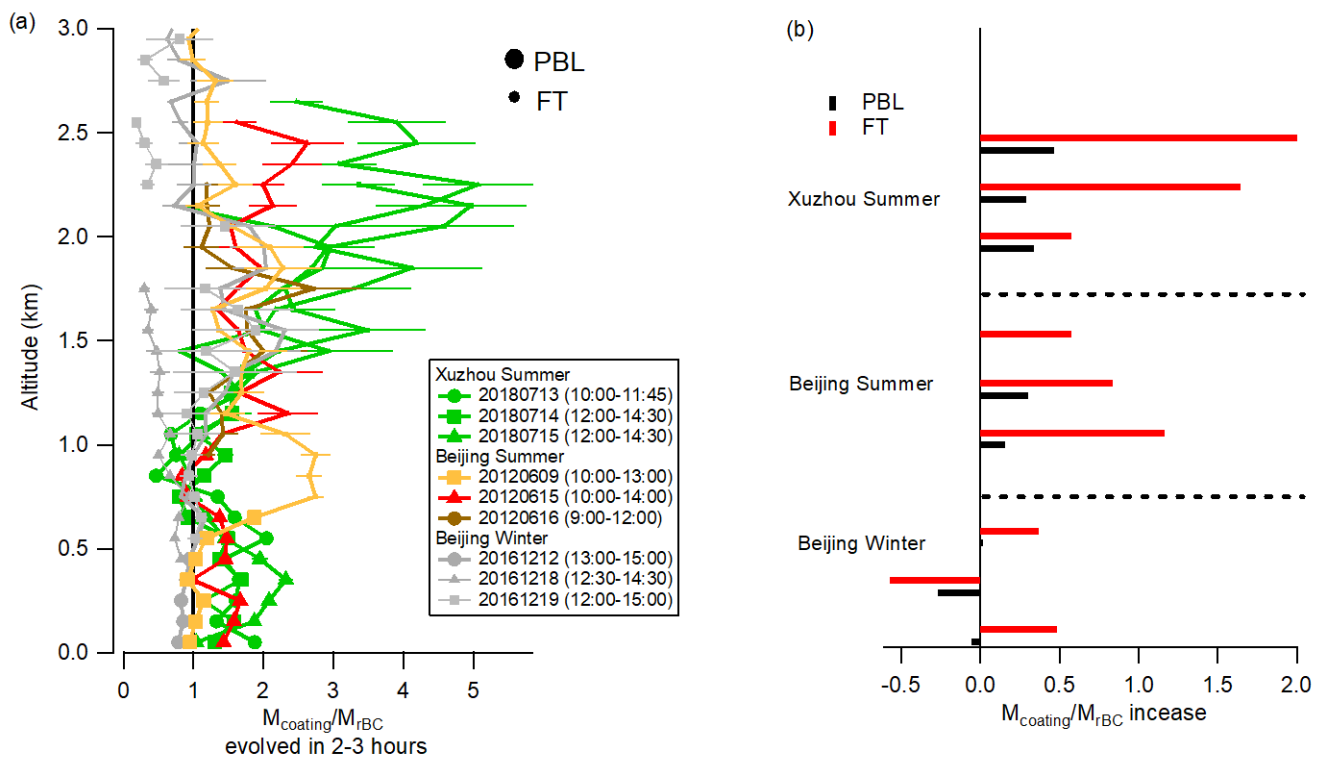
318



319

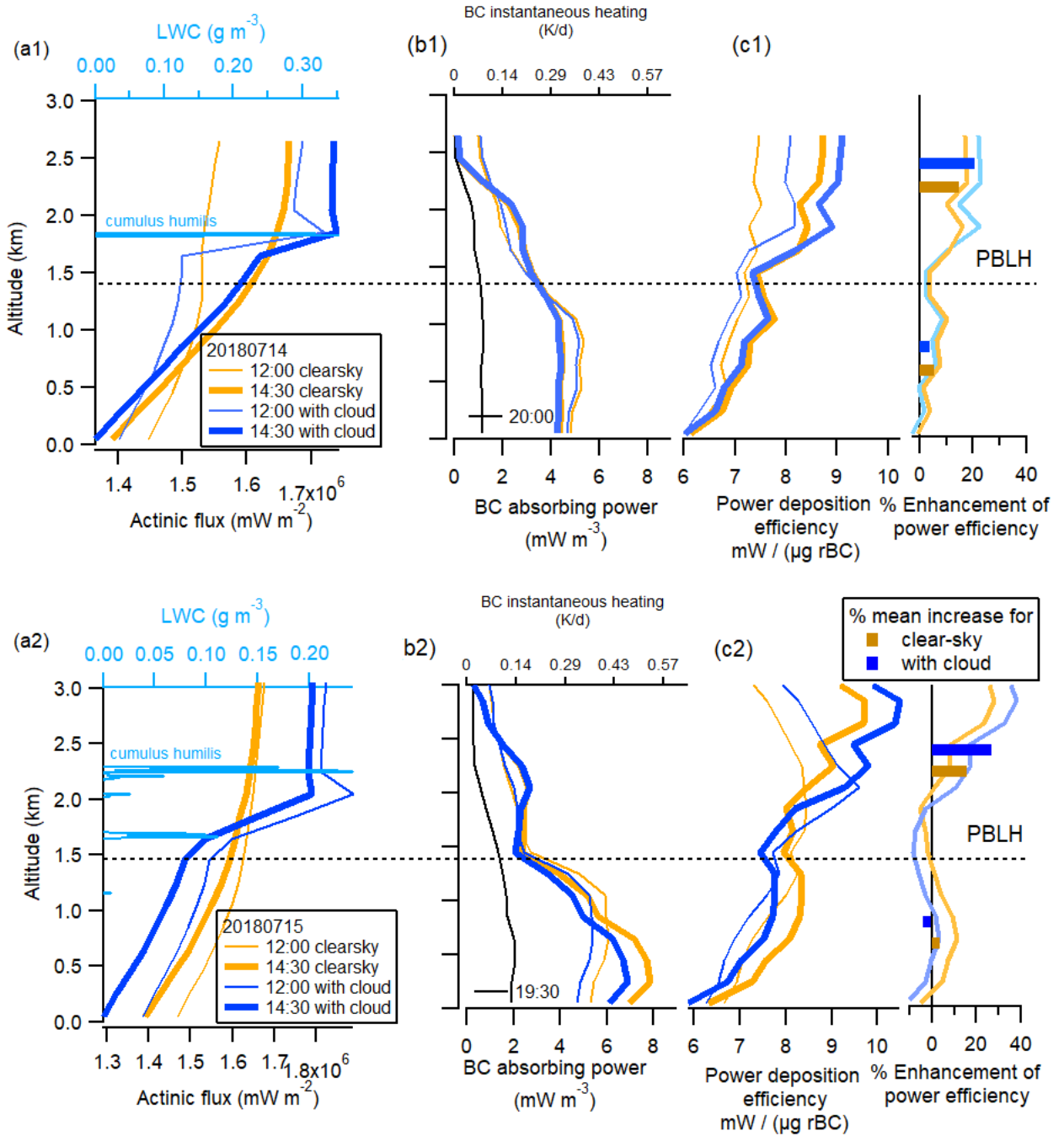
320 Fig. 3. Vertical profiles of BC-related properties during Xuzhou summer campaign. (a) rBC mass  
 321 loading, (b) mass ratio of PM<sub>1</sub>/rBC, (c) mass ratio of coating/rBC ( $M_{\text{coating}}/M_{\text{rBC}}$ ), and (d) BC mass  
 322 absorption cross section ( $\text{MAC}_{550}$ ) and absorption enhancement all profiles in 0714 and 0715. The  
 323 dash lines show the PBLH for each profile. The lines and error bars show mean $\pm\sigma$  at each altitude  
 324 bin. The large and small markers denote the planetary boundary layer (PBL) and free troposphere  
 325 (FT) respectively.

326



327

328 Fig. 4. The ratio of  $M_{\text{coating}}/M_{\text{rBC}}$  in 2-3 hours processing (return profile divided by departure profile)  
 329 for Xuzhou 2018 summer, Beijing 2016 winter and 2012 summer campaigns in (a). The large markers  
 330 denote the PBL. The time in bracket denote the time of departure and return profiles for each flight.  
 331 (b) shows the mean increase of  $M_{\text{coating}}/M_{\text{rBC}}$  in the PBL and FT respectively, deducted from the  
 332 results shown in (a).



333

334 Fig. 5. The radiative transfer results during Xuzhou summer campaign. (a) actinic flux in the midday  
 335 and early afternoon with and without cloud (the night flux is  $<10^6$   $\text{mW m}^{-2}$ ), with the blue lines  
 336 showing the FCDP-measured LWC. (b) BC absorbing power and instantaneous heating rate. (c)  
 337 Power efficiency deposited on BC, and its increasing rate in percentage from midday to early  
 338 afternoon. The dash lines show the height of planetary boundary layer (PBLH). The bars on the right  
 339 panels show the mean % enhancement of power efficiency within and above the PBL for clear-sky  
 340 and with-cloud conditions respectively.

341

342



343 **Acknowledgment**

344 This research was supported by the National Key Research and Development Program of China  
345 (2016YFA0602001), National Natural Science Foundation of China (41605108, 41875167,  
346 41875044, 41505128, 41505129, 41775138, 41807313). Processed data is downloadable from the  
347 link (<https://pan.baidu.com/s/1NgHxiBcPKUeSNeJVofmsbQ>) by using extracting code 57wX.

348

349

350 **References**

- 351 Babu, S. S., et al., 2002. Aerosol radiative forcing due to enhanced black carbon at an urban site in India.  
352 *Geophysical Research Letters*. 29, 27-1-27-4.
- 353 Bond, T. C., Bergstrom, R. W., 2006. Light absorption by carbonaceous particles: An investigative review.  
354 *Aerosol science and technology*. 40, 27-67.
- 355 Brioude, J., et al., 2009. Effect of biomass burning on marine stratocumulus clouds off the California coast.  
356 *Atmospheric Chemistry and Physics*. 9, 8841-8856.
- 357 Cross, E. S., et al., 2007. Laboratory and ambient particle density determinations using light scattering in  
358 conjunction with aerosol mass spectrometry. *Aerosol science and technology*. 41, 343-359.
- 359 Ding, A., et al., 2016. Enhanced haze pollution by black carbon in megacities in China. *Geophysical Research*  
360 *Letters*. 43, 2873-2879.
- 361 Donahue, N., et al., 2006. Coupled partitioning, dilution, and chemical aging of semivolatile organics.  
362 *Environmental Science & Technology*. 40, 2635-2643.
- 363 Draxler, R. R., Hess, G., 1998. An overview of the HYSPLIT\_4 modelling system for trajectories. *Australian*  
364 *Meteorological Magazine*. 47, 295-308.
- 365 Emde, C., et al., 2016. The libRadtran software package for radiative transfer calculations (version 2.0. 1).  
366 *Geoscientific Model Development*. 9, 1647-1672.
- 367 Hu, Y., Stamnes, K., 1993. An accurate parameterization of the radiative properties of water clouds suitable  
368 for use in climate models. *Journal of climate*. 6, 728-742.
- 369 Jacobson, M. Z., 2012. Investigating cloud absorption effects: Global absorption properties of black carbon,  
370 tar balls, and soil dust in clouds and aerosols. *Journal of Geophysical Research: Atmospheres*. 117.
- 371 Johnson, B. T., et al., 2004. The semi-direct aerosol effect: Impact of absorbing aerosols on marine  
372 stratocumulus. *Quarterly Journal of the Royal Meteorological Society*. 130, 1407-1422.
- 373 Koch, D., Del Genio, A., 2010. Black carbon semi-direct effects on cloud cover: review and synthesis.  
374 *Atmospheric Chemistry and Physics*. 10, 7685-7696.
- 375 Lamb, K. D., et al., 2018. Estimating Source Region Influences on Black Carbon Abundance, Microphysics,  
376 and Radiative Effect Observed Over South Korea. *Journal of Geophysical Research: Atmospheres*.  
377 123.
- 378 Liu, D., et al., 2014. Size distribution, mixing state and source apportionment of black carbon aerosol in  
379 London during wintertime. *Atmospheric Chemistry and Physics*. 14, 10061-10084.
- 380 Liu, D., et al., 2015. The effect of complex black carbon microphysics on the determination of the optical  
381 properties of brown carbon. *Geophysical Research Letters*. 42, 613-619.
- 382 Liu, D., et al., 2017. Black-carbon absorption enhancement in the atmosphere determined by particle  
383 mixing state. *Nature Geoscience*. 10, 184-188.
- 384 Liu, Q., et al., 2018. A study of elevated pollution layer over the North China Plain using aircraft  
385 measurements. *Atmospheric Environment*. 190, 188-194.
- 386 Nenes, A., et al., 2002. Black carbon radiative heating effects on cloud microphysics and implications for the

387 aerosol indirect effect 2. Cloud microphysics. *Journal of Geophysical Research: Atmospheres*. 107.  
388 Norris, J. R., Wild, M., 2009. Trends in aerosol radiative effects over China and Japan inferred from  
389 observed cloud cover, solar “dimming,” and solar “brightening”. *Journal of Geophysical Research:*  
390 *Atmospheres*. 114.

391 O’Connor, D., et al., Upgrades to the FSSP-100 electronics. International Conference on Clouds and  
392 Precipitation, Cancun, Mexico.[Available at [http://convention-center.net/iccp2008/abstracts/Program\\_on\\_line/Poster\\_13/O-Connor\\_extended\\_final.pdf](http://convention-center.net/iccp2008/abstracts/Program_on_line/Poster_13/O-Connor_extended_final.pdf), 7–11 July.],  
393 2008.  
394

395 Peng, J., et al., 2016. Markedly enhanced absorption and direct radiative forcing of black carbon under  
396 polluted urban environments. *Proceedings of the National Academy of Sciences*. 201602310.

397 Prabha, T. V., Hoogenboom, G., 2009. Observed dimming effect during a forest fire in the southeastern  
398 United States and the role of aerosols. *Geophysical Research Letters*. 36.

399 Ramanathan, V., Carmichael, G., 2008. Global and regional climate changes due to black carbon. *Nature*  
400 *geoscience*. 1, 221-227.

401 Schwarz, J., et al., 2006. Single - particle measurements of midlatitude black carbon and light - scattering  
402 aerosols from the boundary layer to the lower stratosphere. *Journal of Geophysical Research:*  
403 *Atmospheres (1984 – 2012)*. 111.

404 Schwarz, J. P., et al., 2009. Heating rates and surface dimming due to black carbon aerosol absorption  
405 associated with a major U.S. city. *Geophysical Research Letters*. 36, n/a-n/a.

406 Streets, D. G., et al., 2006. Two - decadal aerosol trends as a likely explanation of the global  
407 dimming/brightening transition. *Geophysical Research Letters*. 33.

408 Ting, Y., et al., 2018. The Mixing State of Carbonaceous Aerosols of Primary Emissions from 'Improved'  
409 African Cookstoves. *Environ Sci Technol*.

410 Zhao, D., et al., 2019. Vertical characteristics of black carbon physical properties over Beijing region in warm  
411 and cold seasons. *Atmospheric Environment*.

412 Zhao, D., et al., 2015. In-situ aircraft measurements of the vertical distribution of black carbon in the lower  
413 troposphere of Beijing, China, in the Spring and Summer Time. *Atmosphere*. 6, 713-731.

414